

GALAXY CLUSTER SCALING RELATIONS MEASURED WITH APEX-SZ

A. N. BENDER¹, J. KENNEDY¹, P. A. R. ADE², K. BASU³, F. BERTOLDI³, S. BURKUTEAN³, J. CLARKE^{4,5}, D. DAHLIN⁶,
M. DOBBS¹, D. FERRUSCA⁷, D. FLANIGAN⁴, N. W. HALVERSON^{8,9}, W. L. HOLZAPFEL⁴, C. HORELLOU⁶, B. R. JOHNSON⁴,
Z. D. KERMISH¹⁰, M. KLEIN³, R. KNEISSL^{11,12}, T. LANTING¹, A. T. LEE^{4,13}, J. MEHL⁴, K. M. MENTEN¹⁴, D. MUDERS¹⁴,
A. NAGARAJAN³, F. PACAUD³, C. L. REICHARDT⁴, P. L. RICHARDS⁴, R. SCHAAF³, D. SCHWAN⁴, M. W. SOMMER³,
H. SPIELER¹³, C. TUCKER², B. WESTBROOK⁴

Submitted to the Astrophysical Journal

ABSTRACT

We present thermal Sunyaev-Zel'dovich effect (SZE) measurements for 42 galaxy clusters observed at 150 GHz with the APEX-SZ experiment. For each cluster, we model the pressure profile and calculate the integrated Comptonization Y to estimate the total thermal energy of the intracluster medium (ICM). We compare the measured Y values to X-ray observables of the ICM from the literature (cluster gas mass M_{gas} , temperature T_X , and $Y_X = M_{\text{gas}} T_X$) that relate to total cluster mass. We measure power law scaling relations, including an intrinsic scatter, between the SZE and X-ray observables for both the X-ray selected and uniform REFLEX-DXL cluster sample and the full *ad hoc* APEX-SZ sample. We observe that the lack of uniform X-ray analysis for the full cluster sample introduces significant variability into the measured scaling relations and dominates the level of intrinsic scatter. For the REFLEX-DXL sample, we find results consistent with a self-similar model of cluster evolution dominated by gravitational effects. Comparing to predictions from numerical simulations, these scaling relations prefer models that include cooling and feedback in the ICM. Lastly, we find that the $Y - Y_X$ scaling relation has the lowest measured intrinsic scatter.

Subject headings: galaxies: clusters: intracluster medium – cosmic background radiation – cosmology: observations

1. INTRODUCTION

As the largest gravitationally collapsed objects in the Universe, clusters of galaxies provide a unique opportunity to study the evolution of large-scale structure. The distribution and abundance of clusters is sensitive to both the geometry of the universe and the growth of density perturbations (e.g., Haiman et al. 2001; Weller et al. 2002). Currently, cluster-based constraints on cos-

mology are limited by systematic uncertainties in relating observables to cluster masses. Most of the cluster mass is in the form of dark matter and therefore is not directly observable. Instead, cluster masses are inferred through scaling relations with observable signals such as X-ray luminosity, galaxy velocity distribution, weak-lensing shear and Sunyaev-Zel'dovich effect (SZE) brightness.

Under the model of self-similarity, where cluster evolution is dominated by gravitational processes, cluster mass scales with observable signals through simple power law relations (Kaiser 1986). In this model, the intracluster medium (ICM) is in hydrostatic equilibrium, for which the scaling to cluster mass can be predicted for a given observable. However, self-similarity does not take into account the role of non-thermal mechanisms such as turbulent gas motions in estimating cluster mass. This simple model also neglects the effects of physical processes internal to the cluster such as feedback from active galactic nuclei and star formation. Numerical simulations predict that while the power law exponent of the scaling relations will be consistent with self-similarity, the normalization does depend on the internal cluster astrophysics (Motl et al. 2005; Nagai 2006; Lau et al. 2009). An empirical measurement of the scaling relations therefore informs models of cluster astrophysics, progressing towards the needed calibration for cosmology.

Currently, cluster surveys are operating in the optical (e.g., Gilbank et al. 2011), X-ray (e.g., Vikhlinin et al. 2009b; Mantz et al. 2010b), and the millimeter (e.g., Carlstrom et al. 2011; Swetz et al. 2011; Planck Collaboration XXIX 2013) wavelength regimes. However, optical and X-ray measurements of clusters suffer from cosmological dimming, and only the brightest and most massive clusters are detected at high redshifts

¹ Department of Physics, McGill University, Montréal, Canada, H3A 2T8

² School of Physics and Astronomy, Cardiff University, CF24 3YB Wales, UK

³ Argelander Institute for Astronomy, Bonn University, Bonn, Germany

⁴ Department of Physics, University of California, Berkeley, CA, 94720

⁵ Materials Sciences Division, Lawrence Berkeley National Laboratory, Berkeley, CA, 94720

⁶ Dept. of Earth & Space Sciences, Chalmers University of Technology, Onsala Space Observatory, SE-439 92 Onsala, Sweden

⁷ Instituto Nacional de Astrofísica, Óptica y Electrónica, Luis Enrique Erro 1, Tonantzintla, Puebla, C.P. 72840 México

⁸ Center for Astrophysics and Space Astronomy, Department of Astrophysical and Planetary Sciences, University of Colorado, Boulder, CO, 80309

⁹ Department of Physics, University of Colorado, Boulder, CO, 80309

¹⁰ Department of Physics, Princeton University, Princeton, NJ, 08544

¹¹ European Southern Observatory, Alonso de Córdova 3107, Vitacura, Santiago, Chile

¹² Atacama Large Millimeter/submillimeter Array, Joint ALMA Observatory, Alonso de Córdova 3107, Vitacura, Santiago, Chile

¹³ Physics Division, Lawrence Berkeley National Laboratory, Berkeley, CA, 94720

¹⁴ Max Planck Institute for Radio Astronomy, 53121 Bonn, Germany

($z > 1$). In contrast, the millimeter-wavelength thermal SZE (Sunyaev & Zel'dovich 1972), where Cosmic Microwave Background (CMB) photons inverse-Compton scatter off hot intracluster electrons, is approximately redshift-independent. SZE surveys with sufficient resolution to resolve clusters, such as those performed with the South Pole Telescope (Reichardt et al. 2013) and the Atacama Cosmology Telescope (Hasselfield et al. 2013) detect clusters with a mass selection nearly independent of redshift.

Precision cosmology requires that mass-observable scaling relations be characterized with a high level of accuracy, including both the measurement uncertainty and the intrinsic scatter from cluster-to-cluster differences. Numerical simulations suggest that SZE observations are relatively insensitive to the details of cluster astrophysics compared to their X-ray and optical counterparts (e.g., Hallman et al. 2006; Nagai 2006). Thus, the intrinsic scatter in the SZE scaling relations is expected to be significantly reduced, resulting in a tighter constraint on cluster mass. Previous measurements of SZE scaling relations include interferometric observations from the OVRO/BIMA (Bonamente et al. 2008) and SZA (Culverhouse et al. 2010; Marrone et al. 2012) arrays as well as imaging studies with the South Pole Telescope (Andersson et al. 2011; Plagge et al. 2010; Benson et al. 2013), BOLOCAM (Sayers et al. 2011), Atacama Cosmology Telescope (Marriage et al. 2011), and the Planck mission (Planck Collaboration XI 2011). In general, those studies find that observational SZE scaling relations agree with expectations based on self-similarity and that simulations including additional non-adiabatic physics are preferred.

While cluster samples selected from large surveys (both SZE and X-ray) have well-known selection functions, studies such as the one presented in this paper that target known clusters often select them in an *ad hoc* manner. The influence of this sample selection on SZE scaling relations is unknown. Additionally, the dynamical state of clusters could have a systematic effect on the measured scaling relation. Numerical simulations suggest that the same scaling relations hold regardless of cluster dynamical state (Wik et al. 2008; Krause et al. 2012). Marrone et al. (2012) and Sifón et al. (2013) find results consistent with this prediction for scaling relations comparing the SZE signal with optical mass estimates from weak-lensing and velocity dispersion measurements, respectively. Sifón et al. (2013) also find increased intrinsic scatter for dynamically disturbed clusters.

In this paper, we study how the SZE signal scales with X-ray observables related to cluster mass using observations from the APEX-SZ imaging bolometer array. We measure SZE scaling relations using X-ray observables (Y_X , M_{gas} , and T_X) as proxies for the total cluster mass. APEX-SZ observed a small set of 11 clusters selected from the REFLEX X-ray survey (referred to as the REFLEX-DXL sample (Zhang et al. 2006)) as well as an additional 31 clusters selected in an *ad hoc* manner. For both samples, we compare our measured power laws to the expectations of the self-similar model as well as numerical simulations that incorporate different physical processes in the ICM. We compare the results between the two cluster samples to investigate the effects of sample selection and uniform analysis on the mea-

sured power law and intrinsic scatter of the SZE scaling relations. Lastly, we examine the impact of cluster dynamical state on the measurement of the SZE signal and its relationship to the X-ray observables. In this paper, we assume the WMAP7+BAO+ H_0 Λ CDM best-fit cosmology in which $H_0 = 70.4$ km/s/Mpc, $\Omega_M = 0.272$, and $\Omega_\Lambda = 0.728$ (Komatsu et al. 2011).

The structure of the paper is as follows. Section 2 reviews the SZE and the associated scaling relations. Section 3 introduces the clusters in this study and observations thereof. Section 4 briefly describes the data reduction process for the APEX-SZ instrument. We present the SZE-X-ray scaling relations and discuss these results in Section 5. A summary and an outlook on future work are provided in Section 7.

2. THE THERMAL SUNYAEV-ZEL'DOVICH EFFECT

The SZE occurs when photons from the CMB inverse Compton scatter off hot electrons in the intracluster medium to higher energies (Sunyaev & Zel'dovich 1972). This process distorts the CMB blackbody spectrum with an amplitude proportional to the gas pressure integrated along the line-of-sight. In units of temperature the change is

$$\frac{\Delta T_{\text{SZE}}}{T_{\text{CMB}}} = f(x, T_e) \cdot \int n_e \sigma_T \frac{k_B T_e}{m_e c^2} dl \equiv f(x, T_e) \cdot y, \quad (1)$$

where n_e and T_e are the electron density and temperature of the ICM, T_{CMB} is the temperature of the CMB, σ_T is the Thomson cross-section, k_B is the Boltzmann constant, and $m_e c^2$ is the electron rest mass energy. The integrated pressure is often parametrized in terms of the Comptonization, y . The frequency dependence $f(x, T_e)$ is given by

$$f(x, T_e) = \left(x \frac{e^x + 1}{e^x - 1} - 4 \right) (1 + \delta_{\text{SZE}}(x, T_e)), \quad (2)$$

where $x = h\nu/k_B T_{\text{CMB}}$ and $\delta_{\text{SZE}}(x, T_e)$ is a correction for relativistic electrons (see, e.g., Nozawa et al. 2000). For frequencies below 217 GHz, the SZE manifests itself as a decrement in the CMB spectrum, while at frequencies above 217 GHz the SZE results in an increment. Equation 1 demonstrates two important characteristics of the SZE. First, the SZE is essentially redshift independent since its surface brightness is expressed as a fractional change in the CMB temperature. Second, the dependence on integrated pressure directly measures the thermal energy of the ICM.

The Comptonization integrated over the solid angle of the cluster on the sky,

$$Y = \int y d\Omega, \quad (3)$$

measures the total thermal energy of a cluster, and is therefore expected to be a robust proxy for total mass. In this work, we integrate a parametric model of Y to a radius of r_{500} , the radius at which the mean matter density of the cluster is 500 times the critical density of the Universe, $\rho_c(z) = 3H_0^2 E(z)^2 / 8\pi G$. Assuming that clusters are in hydrostatic equilibrium, the integrated Comptonization scales as a function of the ICM properties according to

$$Y d_A^2 \propto f_{\text{gas}} T_e^{5/2} E(z)^{-1}$$

$$Y d_A^2 \propto f_{\text{gas}}^{-2/3} M_{\text{gas}}^{5/3} E(z)^{2/3}, \quad (4)$$

where $E(z)$ is the expansion rate of the universe normalized to its present value, $E(z) = H(z)/H_0 = \sqrt{\Omega_M(1+z)^3 + \Omega_\Lambda}$, f_{gas} is the gas mass fraction, and d_A is the angular diameter distance of the cluster (Bonamente et al. 2008). A third proxy for cluster mass can be constructed from the combination of temperature and gas mass, $Y_X = M_{\text{gas}} T_X$ (Kravtsov et al. 2006). Y scales with Y_X as

$$Y d_A^2 \propto Y_X, \quad (5)$$

and is expected to have lower intrinsic scatter than $Y - T$ or $Y - M_{\text{gas}}$ due to the anti-correlation of systematic deviations between T and M_{gas} .

3. OBSERVATIONS

APEX-SZ (Schwan et al. 2011) was a transition-edge-sensor (TES) bolometer array located on the 12-meter Atacama Pathfinder Experiment (APEX) telescope in northern Chile (Güsten et al. 2006). The focal plane comprised a total of 280 bolometers distributed on six wafers which were cooled with closed-cycle refrigerators to an average operating temperature of ~ 300 mK and read out using frequency domain multiplexing (Dobbs et al. 2012). The APEX-SZ experiment imaged SZE decrements at 150 GHz with arcminute resolution over a $23'$ field of view (FOV). Additional details of the APEX-SZ instrument are presented in Dobbs et al. (2006) and Schwan et al. (2011).

APEX-SZ completed two commissioning and seven observing runs from 2005 to 2010. During this time, APEX-SZ observed the 42 clusters presented here for a total of approximately 760 hours. APEX-SZ executed a circular drift scan pattern that concentrated the integration time in a region around the known cluster coordinates while limiting overhead time due to telescope turn-arounds. The telescope repeated the circular scan while centered on a constant azimuth and elevation, allowing the target to drift through the FOV. After completing between 11 and 20 circles (4–7 seconds per circle), the telescope slewed to track the target and then repeated the circular pattern. The radius of each circle ($6'$ – $12'$) was chosen from the expected radial extent of each cluster to ensure that the detectors observed the sky background during each scan. These scans resulted in a sky coverage area of approximately $0.75^\circ \times 1.0^\circ$.

Clusters were targeted based on the availability of published X-ray measurements. In general, massive clusters ($T_X > 6$ keV) were selected and the sample included both dynamically relaxed and disturbed clusters. Additionally, APEX-SZ targeted clusters from the REFLEX-DXL X-ray sample (Zhang et al. 2006), which is discussed in further detail in 5.3. Coordinates and map depth for each cluster are given in Table 1.

4. APEX-SZ DATA ANALYSIS

Raw APEX-SZ timestream data contain the faint SZE cluster signal, scan synchronous signals due to ground pick-up and instrumental thermal fluctuations, atmospheric fluctuations, and instrument noise. In order to measure the SZE surface brightness accurately, the array properties must be well characterized and contamination cleaned from the data.

4.1. Beams and Calibration

The beam position and shape for each bolometer in the focal plane are measured from a daily raster scan of a calibration target (Mars, Uranus, or Saturn¹). In addition to the $58''$ FWHM Gaussian main beam, APEX-SZ beams exhibit significant sidelobes (Schwan et al. 2011). We characterize the sidelobes by mapping the individual detector beams and combining them into a composite beam. The total beam area, including the Gaussian main beam and the sidelobes, is then taken into account during further calibration. The beam size is also corrected to account for the angular extent of the source and detector saturation effects.

Absolute flux calibration is performed based on the overall amplitude of response for each detector from a raster scan on a known celestial source. APEX-SZ observed two primary flux calibrators: Mars and Uranus. The planetary disk size and brightness temperature are taken from the Rudy model for Mars (Rudy et al. 1987; Muhleman & Berge 1991) and from the JCMT FLUXES² model for Uranus. As described in Halverson et al. (2009), we refine the absolute brightness temperatures for Mars and Uranus using WMAP results (Hinshaw et al. 2009; Weiland et al. 2011) to improve calibration accuracy. We find that the Rudy temperatures are systematically higher than WMAP by a factor of 1.052 ± 0.01 . The calculation of this factor includes the extrapolation of the Rudy and WMAP 94 GHz brightness temperatures to 150 GHz, 1.016 ± 0.009 , which is included in the total calibration uncertainty. Similarly, we use the data of Griffin & Orton (1993) to extrapolate the WMAP7 94 GHz measurement of Uranus to $T_{150\text{GHz}} = 100.4 \pm 5.3$ K.

Several times during observations primary planetary calibrators were unavailable due to angular proximity to the Sun. The stable Galactic H II regions RCW38 and IRAS12073-6233 were used as secondary calibrators during these periods, with brightness temperatures bootstrapped from back-to-back scans of the primary and secondary calibrators.

The measured calibration is corrected for differences in atmospheric opacity between the data and calibration scans using the measured value of precipitable water vapor (PWV) from the APEX radiometer. Following Sayers et al. (2011), we extrapolate the atmospheric optical depth based on the ATM model (Pardo et al. 2001) and correct accordingly.

In addition to the calibration scan, routine pointing scans of bright quasars are performed throughout the night. We find an average pointing jitter of approximately 5.7 arcseconds in both azimuth and elevation. This is significantly less than the size of the APEX-SZ beam and has a negligible effect on the measurements presented here.

Combining the corrections discussed in this section (beam solid angle, calibrator temperature, atmospheric opacity) with the uncertainty in the frequency band center (see Halverson et al. (2009)) we estimate the uncertainty in the flux calibration to be $\pm 8\%$.

¹ Saturn is used solely to measure beam profiles. It is not used for absolute flux calibration as its large signal can saturate the APEX-SZ bolometers.

² <http://www.jach.hawaii.edu/jac-bin/planetflux.pl>

Table 1
Summary of cluster properties.

Cluster Name	Right Ascension (<i>h m s</i>)	Declination (<i>° ' "</i>)	redshift	Map Depth ^a (μK CMB)
Abell 2744	00 14 18.6	-30 23 15.4	0.307	12
Abell 2813	00 43 24.5	-20 37 31.2	0.292	21
Abell 209	01 31 52.6	-13 36 35.5	0.209	16
XLSS J022145.2-034617	02 21 45.2	-03 46 17.4	0.430	7
RXCJ0232.2-4420	02 32 18.8	-44 20 51.9	0.284	17
Abell 383	02 48 03.3	-03 31 43.6	0.187	14
RXCJ0437.1+0043	04 37 09.5	+00 43 54.5	0.284	14
MS0451.6-0305	04 54 11.3	-03 00 52.6	0.550	21
Abell 520	04 54 09.0	+02 55 18.0	0.203	14
RXCJ0516.6-5430	05 16 35.2	-54 30 36.8	0.294	10
RXCJ0528.9-3927	05 28 52.5	-39 28 16.7	0.284	11
RXCJ0532.9-3701	05 32 55.9	-37 01 34.5	0.275	16
Abell 3404	06 45 30.0	-54 13 42.1	0.164	13
1ES 0657-56	06 58 30.2	-55 56 33.7	0.296	19
Abell 907	09 58 21.9	-11 03 48.2	0.160	11
XMMXCSJ095940.8+023111.3	09 59 40.8	+02 31 11.3	0.720	14
RXCJ1023.6+0411	10 23 39.6	+04 11 12.0	0.291	12
MS1054.4-0321	10 56 59.0	-03 37 37.0	0.830	13
MACSJ1115.8+0129	11 15 51.9	+01 29 55.0	0.355	16
Abell 1300	11 31 54.7	-19 55 40.5	0.308	18
RXCJ1206.2-0848	12 06 12.3	-08 48 06.0	0.439	18
XMMUJ1230.3+1339	12 30 16.9	+13 39 04.3	0.975	11
RDCSJ1252-2927	12 52 54.4	-29 27 17.0	1.240	8
MACSJ1311.0-0311	13 11 01.7	-03 10 37.6	0.494	12
Abell 1689	13 11 29.3	-01 20 26.7	0.184	19
RXCJ1347.5-1144	13 47 30.8	-11 45 09.0	0.451	28
MACSJ1359.1-1929	13 59 10.3	-19 29 24.0	0.447	27
Abell 1835	14 01 01.9	+02 52 35.5	0.253	36
RXCJ1504.1-0248	15 04 07.6	-02 48 16.0	0.215	21
Abell 2163	16 15 46.0	-06 08 54.0	0.203	30
Abell 2204	16 32 47.1	+05 34 32.3	0.152	10
MACSJ1931.8-2635	19 31 49.6	-26 34 34.0	0.352	30
RXCJ2011.3-5725	20 11 27.1	-57 25 09.8	0.279	11
RXCJ2014.8-2430	20 14 49.7	-24 30 30.0	0.161	15
MACSJ2046.0-3430	20 46 00.5	-34 30 17.0	0.423	15
RXCJ2214.9-1359	22 14 57.4	-14 00 10.8	0.503	23
XMMXCSJ2215.9-1738	22 15 58.0	-17 38 02.5	1.450	11
XMMUJ2235.3-2557	22 35 20.6	-25 57 42.0	1.393	9
RXCJ2243.3-0935	22 43 21.4	-09 35 43.0	0.447	20
Abell S1077	22 58 48.1	-34 47 59.4	0.313	17
Abell 2537	23 08 22.0	-02 11 30.0	0.297	11
RXCJ2337.6+0016	23 37 37.8	+00 16 15.5	0.278	20

^a Map depth is measured within the central arcminute from the standard deviation of 500 jackknife noise map realizations.

4.1.1. Gain Fluctuations

Ideally, the responsivity of each bolometer is constant despite changing amounts of incident optical power (Lee et al. 1996). However, when a bolometer is biased near the upper edge of the superconducting transition, the responsivity changes as a result of varying optical power from three sources: the elevation dependence of atmospheric airmass, the overall atmospheric opacity, and the power from an astronomical source. The last effect is sub-dominant, but it cannot be neglected for the case of a bright calibrator. For most detectors in the APEX-SZ array, suppression of responsivity is approximately a linear function of incident optical power. However, some channels exhibit more extreme changes.

We measure the responsivity of each bolometer using the elevation(ϵ) dependent signal $d_i \propto A_{\text{csc},i} \csc(\epsilon)$ introduced by the circular scan pattern. This is repeated for every two minutes of data, normalizing by the changing zenith emissivity to measure $A_{\text{csc},i}$. Channels that exhibit strong nonlinear response are discarded from use in further analysis. For the remaining channels, we model

the response as a linear function and use it to correct the absolute flux calibration, discarding data that deviate more than 2.5σ from the best-fit model. Data with extremely large overall correction factors (greater than 50%) are discarded.

We also correct for two second order effects. First, as a bright calibration source is scanned, variable responsivity will slightly distort the measured beam shape. Second, the fractional solid angle of the sidelobes relative to the main beam will be affected.

Based on the rms scatter around the best-fit gain models, we estimate the uncertainty in the responsivity corrections to be $\pm 5\%$. Combining this uncertainty with the calibration uncertainty from the previous section, we find that the total uncertainty in the APEX-SZ temperature calibration is $\pm 10\%$.

4.2. Timestream Processing

The APEX-SZ data set was measured in widely varying atmospheric conditions, a significant challenge when trying to measure the relatively faint SZE signal. In gen-

Table 2
Summary of cluster X-ray properties.

Cluster Name	T_X keV	Ref.	M_{gas} $10^{13} M_\odot$	Ref.	Y_X $10^{13} \text{keV} M_\odot$	Morphology	Ref.
Abell 2744	10.1 ± 0.3	2	10 ± 2	2	101 ± 20	disturbed	2
Abell 2813	7.7 ± 0.3	2	6 ± 1	2	46 ± 8	disturbed	2
Abell 209	7.1 ± 0.3	1	7.8 ± 0.8	1	55.4 ± 6.1	relaxed	1
XLSS J022145.2-034617	$4.8^{+0.6}_{-0.5}$	7	unclassified	...
RXCJ0232.2-4420	7.0 ± 0.3	2	9 ± 2	2	63 ± 14	relaxed	2
Abell 383	4.7 ± 0.2	1	3.3 ± 0.4	1	15.5 ± 2.0	relaxed	1
RXCJ0437.1+0043	5.1 ± 0.3	2	5 ± 1	2	26 ± 5	disturbed	2
MS0451.6-0305	$6.6^{+0.7}_{-0.6}$	11	$12.1^{+0.2}_{-0.2}$	11	$79.7^{+8.5}_{-7.4}$	disturbed	19
Abell 520	7.23 ± 0.23	3	13.7 ± 1.5	3	99.1 ± 11.3	disturbed	16
RXCJ0516.6-5430	7.5 ± 0.3	2	8 ± 2	2	60 ± 15	disturbed	2
RXCJ0528.9-3927	7.2 ± 0.4	2	9 ± 1	2	65 ± 8	disturbed	2
RXCJ0532.9-3701	9.5 ± 0.4	2	6 ± 1	2	57 ± 10	relaxed	2
Abell 3404	7.6 ± 0.3	1	9.0 ± 1.1	1	68.4 ± 8.8	disturbed	1
1ES 0657-56	10.6 ± 0.2	2	18 ± 3	2	191 ± 32	disturbed	2
Abell 907	5.8 ± 0.3	1	4.3 ± 0.5	1	24.9 ± 3.2	disturbed	1
XMMXCSJ095940.8+023111.3	$7.3^{+1.4}_{-0.8}$	9	unclassified	...
RXCJ1023.6+0411	8.38 ± 0.44	3	10.8 ± 1.0	3	90.5 ± 9.6	relaxed	13
MS1054.4-0321	8.3 ± 0.7	14	disturbed	19
MACSJ1115.8+0129	9.20 ± 0.98	3	9.9 ± 1.1	3	91.1 ± 14.0	relaxed	13
Abell 1300	9.2 ± 0.4	2	8 ± 2	2	74 ± 19	disturbed	2
RXCJ1206.2-0848	10.71 ± 1.29	3	21.9 ± 2.9	3	234.5 ± 42.0	relaxed	15
XMMUJ1230.3+1339	$6.0^{+1.6}_{-1.2}$	4	3 ± 1	4	18^{+7}_{-6}	disturbed	4
RDCSJ1252-2927	$6.6^{+1.5}_{-1.2}$	6	$0.66^{+0.09}_{-0.10}$	6	$4.4^{+1.2}_{-1.0}$	disturbed	17
MACSJ1311.0-0311	6.2 ± 0.7	11	$4.6^{+0.1}_{-0.1}$	11	$28.5^{+3.3}_{-3.3}$	relaxed	13
Abell 1689	8.5 ± 0.2	1	10.5 ± 1.4	1	89.2 ± 12.1	relaxed	1
RXCJ1347.5-1144	10.75 ± 0.83	3	24.8 ± 2.7	3	266.6 ± 35.6	relaxed	13
MACSJ1359.1-1929	6.73 ± 0.96	13	relaxed	13
Abell 1835	8.4 ± 0.3	1	11.8 ± 1.4	1	99.1 ± 12.3	relaxed	1
RXCJ1504.1-0248	8.00 ± 0.44	3	12.5 ± 1.3	3	100.0 ± 11.8	relaxed	13
Abell 2163	12.27 ± 0.90	3	44.0 ± 4.5	3	539.9 ± 67.9	disturbed	16
Abell 2204	7.6 ± 0.2	1	8.4 ± 1.0	1	63.8 ± 7.8	relaxed	13
MACSJ1931.8-2635	7.47 ± 1.40	3	11.4 ± 1.5	3	85.2 ± 19.5	relaxed	13
RXCJ2011.3-5725	3.3 ± 0.3	11	3.0 ± 0.1	11	9.8 ± 0.9	disturbed	2
RXCJ2014.8-2430	5.63 ± 0.11	12	$7.1^{+0.1}_{-0.1}$	12	$39.9^{+1.1}_{-1.1}$	relaxed	12
MACSJ2046.0-3430	5.81 ± 1.02	13	relaxed	13
RXCJ2214.9-1359	8.8 ± 0.7	8	relaxed	8
XMMXCSJ2215.9-1738	$7.4^{+2.1}_{-1.4}$	6	0.38 ± 0.09	6	$2.8^{+1.0}_{-0.9}$	unclassified	...
XMMUJ2235.3-2557	$6.0^{+2.5}_{-1.8}$	5	$0.95^{+0.11}_{-0.12}$	6	$5.7^{+2.5}_{-1.9}$	relaxed	18
RXCJ2243.3-0935	8.24 ± 0.92	3	19.8 ± 2.4	3	163.2 ± 26.9	disturbed	15
Abell S1077	8.0 ± 0.5	10	disturbed	10
Abell 2537	7.9 ± 0.7	2	7 ± 1	2	55 ± 9	relaxed	2
RXCJ2337.6+0016	9.6 ± 0.3	2	8 ± 1	2	77 ± 10	disturbed	2

Note. —

1. Zhang et al. (2008) $kT_{(0.2-0.5)r_{500}}$
2. Zhang et al. (2006) $kT_{(0.1-0.5)r_{500}}$
3. Mantz et al. (2010a) $kT_{(0.15-0.5)r_{500}}$
4. Fassbender et al. (2011) $kT_{r < 71''}$
5. Mullis et al. (2005) $kT_{r < 50''}$
6. Culverhouse et al. (2010) $kT_{r < 30''}$
7. Pacaud et al. (2007) $kT_{r < 80''}$
8. Ebeling et al. (2007) $kT_{70kpc < r < r_{1000}}$
9. Mehrrens et al. (2012)
10. De Filippis et al. (2004) $kT_{r < 2.5'}$
11. Maughan et al. (2008) $kT_{(0.15-1)r_{500}}$
12. Pratt et al. (2009) $kT_{(0.15-1)r_{500}}$
13. Allen et al. (2008) $kT_{r < r_{2500}}$
14. Branchesi et al. (2007) $kT_{r < 84''}$
15. Ebeling et al. (2010)
16. Govoni et al. (2004)
17. Demarco et al. (2007)
18. Rosati et al. (2009)
19. Andersson et al. (2009)

eral, the atmospheric signal is highly correlated between bolometers as spatial fluctuations in the atmosphere are much larger than the APEX-SZ FOV. Additionally, the bolometers exhibit a correlated signal due to heating of the detector array from telescope vibrations. We employ several different filtering techniques to clean the data, similar to Halverson et al. (2009). In order to optimize the final maps, filtering is tailored to the specific needs of each target with the goal of sufficiently removing contamination and minimizing noise while preserving cluster signal.

4.2.1. Initial Data Conditioning

The first step to condition APEX-SZ timestreams is to parse the data into separate circles made on the sky according to the scan pattern. The circles are grouped together based on a common central azimuth and elevation and data not in a circle set are discarded.

Initial channel and data cuts are performed on the indexed data based on several criteria. Channels that are optically unresponsive (optical efficiency less than 6%) are rejected. APEX-SZ timestreams occasionally exhibit large spikes or glitches in one or many bolometers due to either cosmic rays or electrical interference. Glitches are located and removed from the timestreams using both the timestream derivative and a simple S/N threshold cut. When a glitch is simultaneously detected in several channels (more than 7%), that particular section of data is discarded for all channels. As a final step, channels with excess noise between 12 and 18 Hz are discarded.

After the initial data cuts we deconvolve an optical time constant for each channel from the timestreams. The median measured optical time constant for APEX-SZ bolometers is ~ 12 ms, however, it is as high as ~ 60 ms for some channels. To prevent the amplification of high frequency noise during deconvolution, an additional low-pass filter ($F = \exp[-(f/f_0)^6]$) is applied. We define $f_0 = 2 * v_{\text{scan}}/\text{FWHM}$ where v_{scan} is the median scan velocity of the telescope and FWHM is the full width at half-maximum of the APEX-SZ beam.

4.2.2. Removal of Timestream Contamination

The final step in processing the timestream data is to remove the dominant atmospheric and thermal signals. The majority of the timestream cleaning is performed through a combination of two methods: high-pass time-domain filters and the subtraction of spatial polynomial functions across the array, taking advantage of the correlation between bolometers.

An initial high-pass filter removes the static offset for each channel as well as low-frequency noise in the timestreams. Removing the timestream signal due to stage heating is especially important because the subsequent spatial template removal steps use relative gain coefficients that are based solely on the atmospheric response. The high-pass filtering is implemented in two forms: an N-order polynomial removal and a Butterworth frequency domain filter. The polynomial filter, described in detail in Halverson et al. (2009), simultaneously removes a scan synchronous cosecant signal.

After the first high-pass filter, we remove a 2-dimensional spatial polynomial function across the array (Sayers 2007; Halverson et al. 2009) at each sample in the

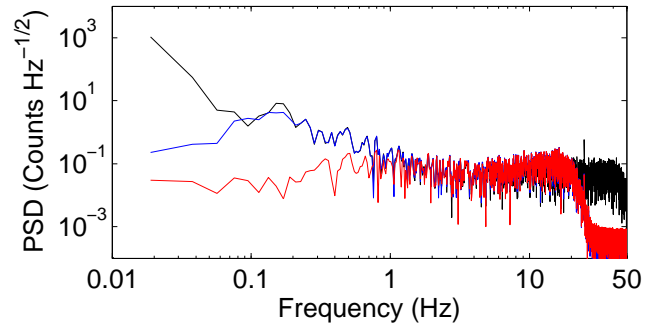


Figure 1. The power spectral density (PSD) of an APEX-SZ timestream at three different stages of timestream reduction. The black line represents the raw data in units of readout counts. The blue line shows the power remaining after initial data cuts are performed, optical time constants are deconvolved, and a high-pass filter is applied. The decrease in low-frequency power is due to the high-pass step, whereas roll-off at high-frequencies is a result of the low-pass filter included in the time constant deconvolution. The red line shows the power spectrum after spatial template removal and polynomial removal steps are performed, removing the remaining low-frequency contamination and completing the cleaning of the data.

timestream. During this process, referred to as *spatial template removal*, we fit the polynomial either across the entire array, or individually for each of the six detector wafers to improve removal of correlated signals on scales smaller than the 0.4° field-of-view. Often, this filter is applied multiple times, discarding channels with excess variance in between. A final polynomial removal is performed to remove any remaining contamination. Figure 1 shows the power spectrum of an APEX-SZ timestream at three different steps in the reduction process.

4.3. Map Making & Transfer Function

Once the timestreams are filtered, we create sky maps by binning the timestream data into 10×10 arcsecond pixels. Sky coordinates for each bolometer are determined from the absolute telescope boresight pointing and individual bolometer positional offsets. As in Halverson et al. (2009), bolometers and scans are combined with a minimum variance weighting for each cluster. The resulting set of 42 sky maps is shown in Figure 2. Each map has been convolved with a one arcminute FWHM Gaussian for visual presentation. However, all subsequent analysis is performed on the unsmoothed version.

In conjunction with the sky map, we quantify the effects of the APEX-SZ instrumental beam and analysis filtering on the sky signal. A simulated cluster map, created using the profile discussed in Section 4.4.1, is convolved with the composite beam profile of the array and mapped into timestreams using the telescope pointing information. Each data cut and filtering process performed on the real cluster data is repeated on these timestreams. The filtered simulation is mapped and coadded using the same minimum variance weights as the cluster map. An individualized transfer function map, \mathbf{K} , is created for each cluster by normalizing the Fourier transform of the filtered map to that of the original simulation.

We create jackknife noise maps for each cluster to characterize the map noise. In this process, random halves of the individual scan maps are multiplied by -1 before coadding. This removes any astrophysical signal that

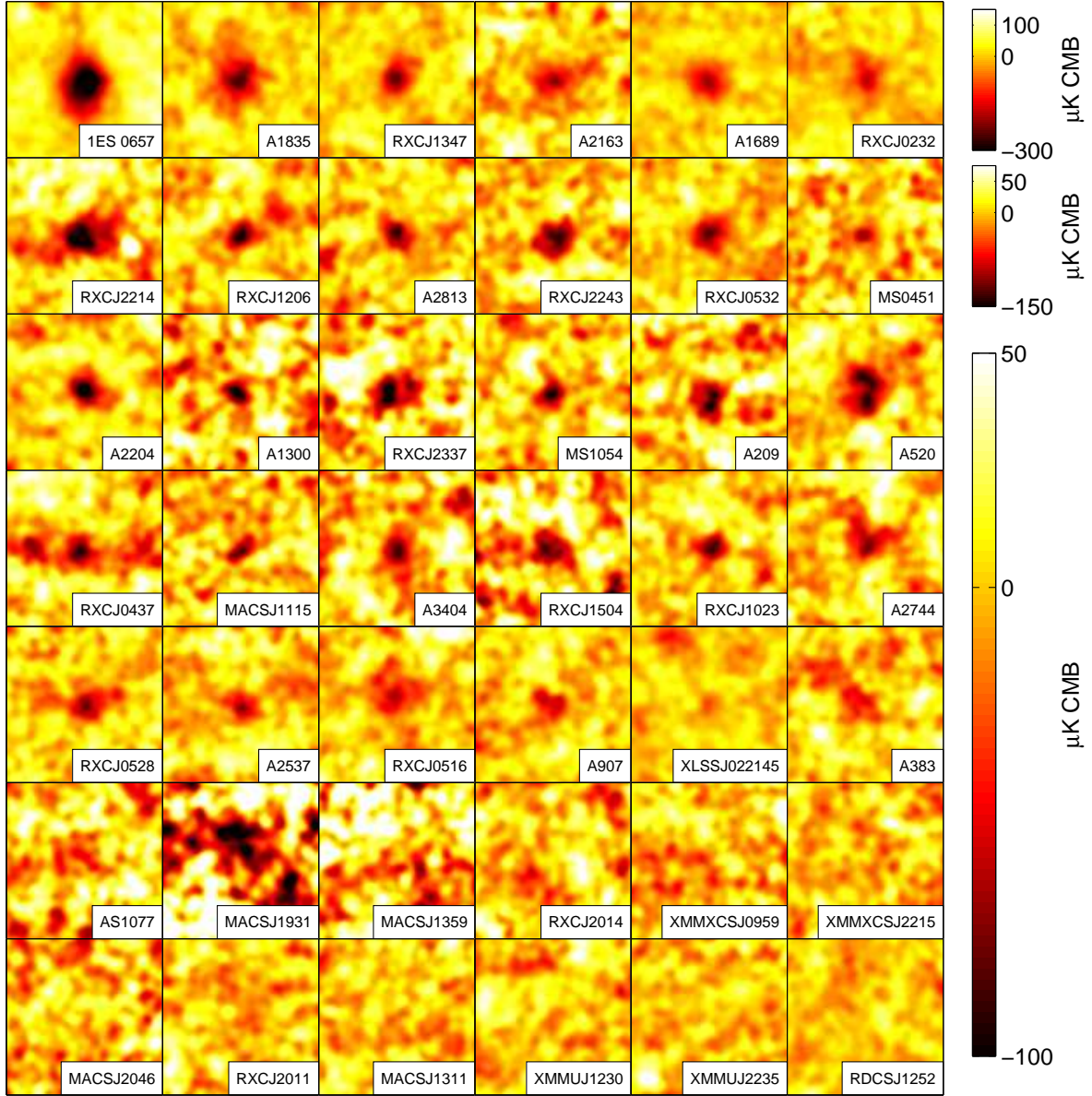


Figure 2. Sky maps for each of the APEX-SZ cluster positions in signal-to-noise units. The data for each 15×15 square arcminute map have been filtered to remove contaminating signals. Therefore, the maps show an attenuated representation of the sky. Each map has been additionally convolved with a one arcminute Gaussian.

is consistent between all maps, including primary CMB anisotropy. To account for the noise due to the CMB, we convolve a realization of the CMB created from the WMAP5 best-fit power spectrum (Nolta et al. 2009) with a CMB transfer function (created in the same way as the cluster transfer function) and add it to the jackknife noise map. In addition to the CMB, a contribution from a background of point sources is expected. We find that the power from Poisson distributed point sources (Hall et al. 2010; Shirokoff et al. 2011), including an extra 50% variance due to lensing (Hezaveh et al. 2013), is negligible in comparison to the instrument noise.

4.4. Cluster Signal Modeling

4.4.1. Parametric Models

In order to calculate the integrated cluster signal, we need to extrapolate the measured cluster signal to spatial scales that have been filtered out due to timestream processing and the angular resolution of the instrument. We adopt the universal pressure profile of Arnaud et al. (2010),

$$P_e(r) = \frac{P_0}{(r/r_s)^\gamma [1 + (r/r_s)^\alpha]^{(\beta-\gamma)/\alpha}}. \quad (6)$$

Here P_0 is the normalization of the pressure profile, r_s is the scale radius, and (α, β, γ) describe the slope of the profile for $r \approx r_s$, $r > r_s$ and $r < r_s$, respectively. The scale radius is often defined in terms of a concentration parameter c_{500} , $r_s = r_{500}/c_{500}$. Proposed by Nagai et al. (2007a), this generalized Navarro-Frenk-White model (GNFW), is a generalization of the numerical results from Navarro et al. (1997) for the distribution of mass in a dark matter halo. Arnaud et al. (2010) combined simulations and X-ray observations to measure a best-fit model of $(c_{500}, \alpha, \beta, \gamma) = (1.177, 1.0510, 5.4905, 0.3081)$, which we use for the measurements presented here. Applying the ideal gas law, $P_e = n_e k T_e$, to Equation 6 and substituting into Equation 1 the SZE profile becomes

$$\frac{\Delta T_{\text{SZE}}}{T_{\text{CMB}}} = f(x, T_e) \cdot \int \frac{\sigma_T}{m_e c^2} P_e(r) dl. \quad (7)$$

We reparametrize Equation 7 in terms of a normalization ΔT_0 ,

$$\Delta T_{\text{SZE}} = \Delta T_0 \int \frac{1}{(r/r_s)^\gamma [1 + (r/r_s)^\alpha]^{(\beta-\gamma)/\alpha}} dl. \quad (8)$$

Due to the compact scan pattern and strong atmospheric filtering required, the APEX-SZ data poorly constrain power on scales larger than 10 arcminutes in the maps. Therefore, we infer r_{500} from the X-ray based $r_{500} - T$ scaling relation of Vikhlinin et al. (2006) for each cluster and fix the model centroid at the X-ray centroid. The Arnaud et al. (2010) profile for each cluster serves as the simulated input for creating the individualized transfer functions described in §4.3 and is used to fit for the normalization, ΔT_0 .

4.4.2. Likelihood Analysis

We calculate the likelihood for each model as a function of ΔT_0 , $\mathcal{L} \propto e^{-\chi^2(\Delta T_0)/2}$. First, we create a 2-dimensional model map $\mathbf{M}(\Delta T_0)$ and convolve it with

the transfer function map \mathbf{K} , $\mathbf{M}'(\Delta T_0) = \mathbf{K} * \mathbf{M}(\Delta T_0)$. The model $\mathbf{M}'(\Delta T_0)$ and sky maps \mathbf{D} are binned into 1-arcminute radial bins around the X-ray centroid. Using the central 10 arcminutes of these profiles, we construct the χ^2 statistic,

$$\chi^2 = (\mathbf{D} - \mathbf{M}'(\Delta T_0))^T \mathbf{C}_n^{-1} (\mathbf{D} - \mathbf{M}'(\Delta T_0)), \quad (9)$$

where \mathbf{C}_n is the noise covariance matrix estimated by averaging 500 radially-binned jackknife noise realizations. The best-fit parameters along with the X-ray based $\theta_{500} = r_{500}/d_A$ and respective probability to exceed (PTE) are given in Table 3.

For each cluster, we calculate the spherical integral of the assumed model profile within the X-ray defined r_{500} and use the measured ΔT_0 to estimate the integrated Comptonization Y_{500} . We use the work of Nozawa et al. (2000) and the X-ray temperatures from Table 2 to calculate the relativistic correction δ_{SZE} to the frequency dependent term in Equation 2. On average, this correction is of order $\sim 5\%$. The measured values of Y_{500} are given in Table 3.

5. RESULTS

5.1. Cluster Observables

We use the method described in Section 4.4 to measure the spherically-integrated Comptonization for each cluster. We assume the cluster follows an Arnaud et al. (2010) pressure profile (see Equation 6) with radius r_{500} , where r_{500} is inferred from the Vikhlinin et al. (2006) $r - T_X$ relation.

We use three different proxies for total cluster mass: spectroscopic X-ray temperature, gas mass, and Y_X , the values for which are taken from the literature. The redshifts and X-ray parameters for the 42 clusters included in this sample are given in Table 2 along with the references. All measurements were made with either the XMM-Newton or Chandra X-ray observatories. X-ray temperatures are used that were derived from temperature maps with the central region excluded when available. Inclusion of the core region can lead to an underestimated global temperature for the cool-core clusters present within our sample. M_{gas} values, and by extension Y_X , were available for only 35 clusters.

5.2. Regression Analysis

To derive best-fit scaling relations parameters we perform a regression analysis of the data shown in Figure 3. We assume that the data follow the power law relationship,

$$Y_{500} d_A^2 E(z)^\delta = A \cdot \left(\frac{X}{X_0} \right)^B, \quad (10)$$

where A is the normalization, B is the power law exponent, and X denotes an X-ray observable. A pivot point, X_0 , is chosen for each observable ($T_0 = 7.5$ keV, $M_{\text{gas},0} = 1.0 \times 10^{14} M_\odot$, $Y_{X,0} = 8.0 \times 10^{14} M_\odot \text{keV}$) to decorrelate A and B . We use the self-similar values of $\delta = (1, -2/3, 0)$, respectively (see Equation 4). The intrinsic astrophysical scatter in the scaling relation is represented through a log-normal distribution with mean $\mu = \log_{10} A + B \cdot \log_{10}(X/X_0)$ and variance $\sigma_{\log_{10}(Y)}^2$ in the base 10 logarithm of the distribution.

Table 3
APEX-SZ Model Fits

Cluster Name	ΔT_0 ($\mu\text{K CMB}$)	θ_{500} ($''$)	PTE	Y_{500} (10^{-10} sr)
Abell 2744 [†]	-460 ± 83	311.3	0.08	1.58 ± 0.28
Abell 2813 [†]	-548 ± 83	281.7	0.19	1.51 ± 0.23
Abell 209	-464 ± 82	360.9	0.25	2.10 ± 0.37
XLSS J022145.2-034617	-231 ± 55	158.6	0.14	0.20 ± 0.05
RXCJ0232.2-4420 [†]	-618 ± 70	274.3	2.1×10^{-3}	1.61 ± 0.18
Abell 383	-275 ± 70	320.5	0.71	0.97 ± 0.25
RXCJ0437.1+0043 [†]	-390 ± 76	232.2	1.6×10^{-4}	0.72 ± 0.14
MS0451.6-0305	-772 ± 177	153.2	0.26	0.63 ± 0.14
Abell 520	-322 ± 52	373.9	5.4×10^{-6}	1.56 ± 0.25
RXCJ0516.6-5430 [†]	-217 ± 60	276.2	8.6×10^{-9}	0.58 ± 0.16
RXCJ0528.9-3927 [†]	-444 ± 68	278.5	2.9×10^{-5}	1.20 ± 0.18
RXCJ0532.9-3701 [†]	-581 ± 77	331.3	4.7×10^{-4}	2.25 ± 0.30
Abell 3404	-486 ± 66	464.4	3.2×10^{-3}	3.65 ± 0.50
1ES 0657-56 [†]	-1183 ± 50	329.5	4.9×10^{-13}	4.53 ± 0.19
Abell 907	-333 ± 50	411.8	0.65	1.95 ± 0.29
XMMXCSJ095940.8+023111.3	-140 ± 107	135.1	5.5×10^{-3}	0.089 ± 0.068
RXCJ1023.6+0411	-453 ± 72	295.7	0.19	1.39 ± 0.22
MS1054.4-0321	-912 ± 124	123.8	0.97	0.49 ± 0.07
MACSJ1115.8+0129	-326 ± 91	262.1	0.17	0.79 ± 0.22
Abell 1300 [†]	-518 ± 103	295.6	0.81	1.59 ± 0.32
RXCJ1206.2-0848	-767 ± 104	237.8	0.27	1.53 ± 0.21
XMMUJ1230.3+1339	-283 ± 124	91.6	0.36	0.082 ± 0.036
RDSCSJ1252-2927*	-20 ± 119	79.2	0.42	$(4.24 \times 10^{-3}) \pm 0.026$
MACSJ1311.0-0311*	-68 ± 88	161.8	0.90	0.061 ± 0.079
Abell 1689	-1041 ± 85	444.3	0.11	7.20 ± 0.59
RXCJ1347.5-1144	-1038 ± 127	233.1	0.15	1.99 ± 0.24
MACSJ1359.1-1929	-184 ± 125	183.5	0.02	0.21 ± 0.15
Abell 1835	-828 ± 121	333.7	0.34	3.23 ± 0.47
RXCJ1504.1-0248	-596 ± 112	374.4	0.51	2.92 ± 0.55
Abell 2163	-681 ± 100	494.0	0.86	5.94 ± 0.87
Abell 2204	-627 ± 55	497.4	0.05	5.40 ± 0.47
MACSJ1931.8-2635*	-16 ± 125	236.6	0.24	0.031 ± 0.244
RXCJ2011.3-5725	-120 ± 91	187.7	0.16	0.14 ± 0.11
RXCJ2014.8-2430*	6 ± 90	403.1	0.57	-0.034 ± 0.502
MACSJ2046.0-3430	-145 ± 123	177.7	0.70	0.16 ± 0.13
RXCJ2214.9-1359	-800 ± 101	191.8	5.2×10^{-5}	1.03 ± 0.13
XMMXCSJ2215.9-1738*	6 ± 181	74.1	0.15	$(-1.15 \times 10^{-3}) \pm 0.035$
XMMUJ2235.3-2557*	-28 ± 190	68.6	0.44	$(4.62 \times 10^{-3}) \pm 0.031$
RXCJ2243.3-0935	-926 ± 117	204.1	0.03	1.35 ± 0.17
Abell S1077	-281 ± 118	270.9	0.06	0.72 ± 0.30
Abell 2537 [†]	-425 ± 78	281.7	0.03	1.18 ± 0.22
RXCJ2337.6+0016 [†]	-402 ± 77	330.1	0.13	1.54 ± 0.29

Note. — Y_{500} is the spherical integration of best-fit pressure profile within r_{500} . Clusters in the REFLEX-DXL subsample are denoted by [†] and non-detections with *.

This regression is often performed in the log basis, where Equation 10 transforms to a simple linear relationship with Gaussian intrinsic scatter. In agreement with Kelly (2007, hereafter K07), we find from simulated data sets that common methods for linear regression with uncertainty in both the x- and y-variables, such as those in Press et al. (2007) and Weiner et al. (2006), introduce systematic bias into the measured parameters. The regression parameters are further biased by the symmetrization and transformation of the Y_{500} likelihood distribution from the linear basis to the logarithmic basis. Lastly, the measured Y_{500} non-detections in the APEX-SZ data cannot be fully represented in the log basis. For example, when we place a prior that $Y_{500} > 0$ and perform a linear regression using the Bayesian method of sampling the posterior probability from K07, we find that the resulting maximum likelihood parameters are biased at the $1 - 2\sigma$ level.

To address the difficulties introduced by the log basis, we instead perform the regression analysis in the linear basis. We construct the likelihood of the scaling relations parameters from the probability densities of Y_{500} measured with APEX-SZ and the X-ray observable (e.g., Y_X). We approximate the measured probabilities in Y_{500} as asymmetric Gaussian distributions. Following the methodology of K07, we model the distribution of X as a weighted sum of Gaussian functions.³ We sample the posterior likelihood distribution using an MCMC method with a Metropolis-Hastings algorithm. Using simulated data sets with X-ray properties based on those of the APEX-SZ cluster sample, we find that we are able to recover unbiased estimates of the scaling relation parameters.

5.3. $Y_{500} - Y_X$, $Y_{500} - M_{\text{gas}}$, $Y_{500} - T_X$ Relations

We fit the three scaling relations described in the previous section for two different cluster samples: the X-ray selected REFLEX-DXL clusters and the full sample of clusters observed by APEX-SZ.

APEX-SZ observed 11 of the 13 clusters from the X-ray selected REFLEX-DXL cluster sample (Zhang et al. 2006). The remaining two clusters were not observed due to restrictions in accessible right ascension and declination. These clusters have an X-ray luminosity $L_X > 5.9 \times 10^{44}$ ergs/s in the ROSAT-ESO Flux Limited X-ray (REFLEX) galaxy cluster survey (Böhringer et al. 2004) and fall within a narrow redshift range, $0.27 < z < 0.31$. Zhang et al. (2006) observed the REFLEX-DXL clusters with the XMM-Newton satellite and measured the X-ray temperature and gas mass for each.

The second sample for which we fit the scaling relations includes all 42 clusters in Table 3. Overall, these clusters were chosen in an *ad hoc* manner. We are unable to quantify the influence of this selection, resulting in an unknown level of systematic bias and uncertainty present in the results for this sample.

The maximum likelihood regression parameters and 68% confidence intervals for both samples are given in Table 4 and shown in Figure 3. We also give results for the cases where we fix the power law exponent to the

self-similar values.

5.3.1. The REFLEX-DXL and Full Cluster Samples

First, we consider our constraints on the power law exponent B for all three scaling relations. We find for the REFLEX-DXL sample that B is consistent with self-similar expectations for all three scaling relations. Similarly, the measured exponent of the $Y_{500} - Y_X$ relation for the full cluster sample is consistent with self-similarity. In contrast, for the full sample $Y_{500} - T_X$ relation we find a marginally steeper power law than expected in the self-similar case and measured for the REFLEX-DXL sample. Randomly sampling sets of 11 clusters from the full cluster sample and performing the regression analysis on each, we find the cumulative probability for an exponent equal to or less than that of the REFLEX-DXL sample to be 0.1%, indicating a real difference between the two samples. We measure the exponent for the full sample $Y_{500} - M_{\text{gas}}$ relation to be consistent with the value for the REFLEX-DXL sample. However, this constraint tightens in comparison to the REFLEX-DXL sample and is significantly less ($> 4\sigma$) than the self-similar expectation.

Next, we examine our measurements of the power law normalization A . The normalization of the $Y_{500} - T_X$ relation is consistent between the two cluster samples, while the $Y_{500} - Y_X$ and $Y_{500} - M_{\text{gas}}$ relations both see a lower normalization for the full sample in comparison to the REFLEX-DXL. We compare our measurements for $Y_{500} - M_{\text{gas}}$ and $Y_{500} - T_X$ to the numerical simulations of Nagai (2006) (see Figures 4 and 5). These simulations agree well with the self-similar model. We therefore find similar tension between the measured $Y_{500} - M_{\text{gas}}$ exponent for both samples and the simulations as for the comparison to self-similarity. Different models of cluster gas physics are expected to influence only the scaling relation normalization. For this reason, despite the tension in the full scaling relation fit, we consider the result where B has been fixed to the self-similar value. As shown in Figures 4 and 5, the $Y_{500} - T_X$ results for both samples and the $Y_{500} - M_{\text{gas}}$ results for the REFLEX-DXL sample favor simulations that include cooling and feedback over those with only standard gas dynamics. In contrast, the lower normalization for the full sample $Y_{500} - M_{\text{gas}}$ relation causes a preference for standard gas dynamics. For both samples, the $Y_{500} - M_{\text{gas}}$ conclusions are weak because of the measured tension in the exponent.

The third free parameter in our regression model, $\sigma_{\log_{10}(Y)}$, quantifies the amount of scatter in the scaling relation not due to measurement uncertainties in $\log_{10}(Y_{500})$. We transform the values of $\sigma_{\log_{10}(Y)}$ from Table 4 into the fractional scatter $\sigma_Y/Y = \sigma_{\log_{10}(Y)}/\log_{10}(e)$. We measure 28% ($\sigma_{\log_{10}(Y)} = 0.12^{+0.07}_{-0.05}$) intrinsic scatter in the $Y_{500} - Y_X$ relation for the REFLEX-DXL sample. Kravtsov et al. (2006) demonstrated that Y_X is a more robust mass proxy than T_X or M_{gas} . Because Y and Y_X measure similar quantities (Equation 5), we expect that $Y_{500} - Y_X$ will have the lowest intrinsic scatter of the three scaling relations. As anticipated, the $Y_{500} - M_{\text{gas}}$ and $Y_{500} - T_X$ scaling relations exhibit increased levels of intrinsic scatter (41%, and 39%, respectively).

For the full APEX-SZ cluster sample, we measure an

³ The MCMC algorithm is largely based on the publicly available IDL code from Kelly (2007) which can be found at: http://idlastro.gsfc.nasa.gov/ftp/pro/math/linmix_err.pro.

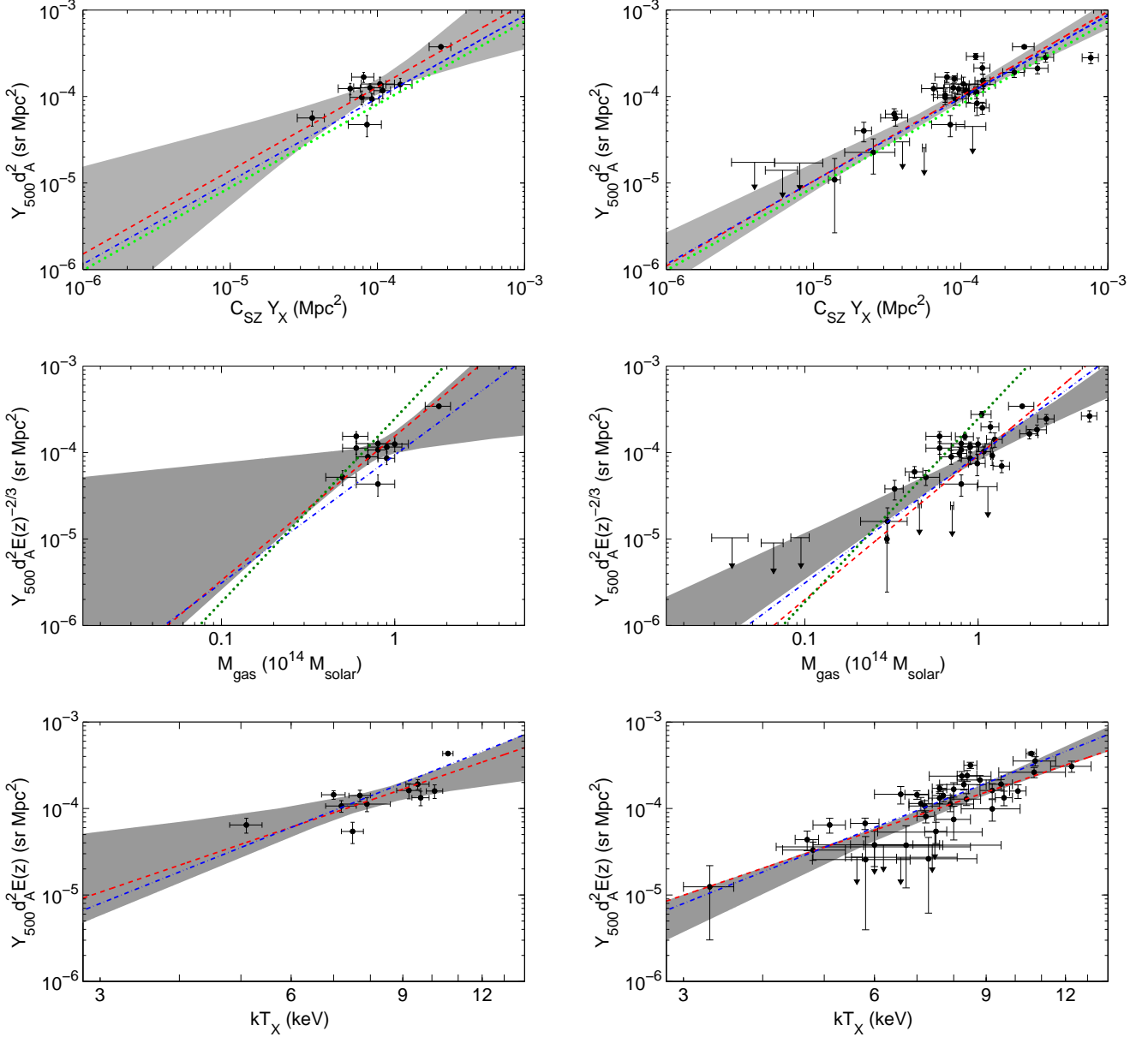


Figure 3. $Y_{500} - Y_X$, $Y_{500} - M_{\text{gas}}$, and $Y_{500} - T_X$ scaling relations for the REFLEX-DXL (left column) and full (right column) cluster samples. The black points show the APEX-SZ measured values given in Table 3. Non-detections are plotted as 95% upper limits. The shaded region depicts the 68% confidence interval of the power law for the three-parameter fit. Also shown is the maximum likelihood result for the case where the exponent is fixed to the self-similar value (red dashed). For comparison, we plot the best-fit results from Planck Collaboration XI (2011) (blue dot-dash), Plagge et al. (2010) (dark green dot), and Andersson et al. (2011) (light green dot).

intrinsic scatter of $46 \pm 6\%$ in $Y_{500} - Y_X$, $55 \pm 7\%$ in $Y_{500} - M_{\text{gas}}$, and $44 \pm 9\%$ in $Y_{500} - T_X$. In all three cases, these measurements agree within uncertainties with the results from the REFLEX-DXL sample. However, this does differ from the REFLEX-DXL sample result where the intrinsic scatter decreased for $Y_{500} - Y_X$ in comparison to $Y_{500} - M_{\text{gas}}$ and $Y_{500} - T_X$, and we investigate this difference in the Section 6.

5.3.2. Comparison with Previous Experiments

There are four main observational studies with which we directly compare our Y_{500} scaling relations. Planck Collaboration XI (2011, hereafter P11) and Planck Collaboration XXIX (2013, hereafter P13) present SZE scal-

ing relations using the Planck satellite (the early and 2013 results, respectively) in combination with X-ray data using the XMM-Newton satellite. Plagge et al. (2010, S10) and Andersson et al. (2011, S11) constrain SZE scaling relations using the South Pole telescope. Results from these studies are compared to the APEX-SZ results in Figure 3.

The APEX-SZ results for the REFLEX-DXL sample agree well with both the P11 and P13 constraints on the $Y_{500} - M_{\text{gas}}$ and $Y_{500} - Y_X$ exponents. S11 explore $Y_{500} - Y_X$ and likewise measure an exponent consistent with the APEX-SZ result. S10 evaluate both $Y_{500} - M_{\text{gas}}$ and $Y_{500} - Y_X$ and measure exponents which are approximately 1.6σ higher than the APEX-SZ val-

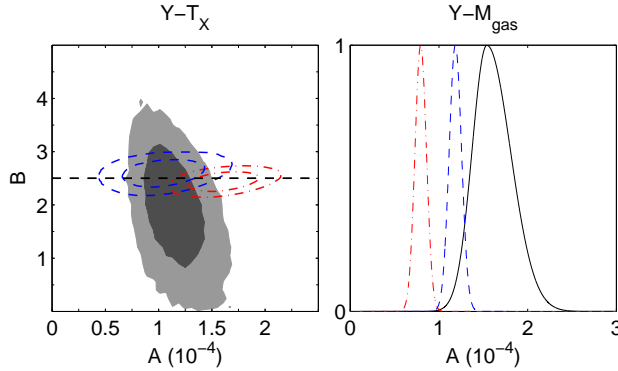


Figure 4. Likelihood constraints for the REFLEX-DXL sample. The two-dimensional constraint for the normalization A and power exponent B is shown for the $Y_{500} - T_X$ relation in the left panel. The grey shaded areas represent the 68% and 95% confidence regions and the dashed straight line shows the self-similar value of the exponent. The $Y_{500} - M_{\text{gas}}$ constraint on A for the case where the exponent is fixed to the self-similar value ($B = 5/3$) is shown in the right panel. For comparison, the numerical results of Nagai (2006) for standard gas dynamics only (red/dash-dot) and cooling and feedback (blue/dashed) are shown in both panels.

ues. However, these authors note that their results vary significantly when using different values of gas mass from the literature.

To compare the measured APEX-SZ power law normalization of the $Y_{500} - Y_X$ relation for the REFLEX-DXL sample (given in Table 4) to previous measurements we transform our normalization parameter to $A' = A \times 10^{-4}/8 \times 10^{14}/C_{\text{SZ}}$, where $C_{\text{SZ}} = \sigma_{\text{th}}/m_e c^2 \mu_e m_p$ (Arnaud et al. 2010). In the case where $B = 1$, the ratio of $A' = Y_{500} d_A^2/Y_x$ is a function of the differences between the mass-weighted and spectroscopic cluster temperatures. We find $A' = 1.28^{+0.19}_{-0.17}$ for the REFLEX-DXL sample. This result has a slight tension with observations that indicate A' is less than unity, including those from S11 ($A' = 0.82 \pm 0.07$) and P13 ($A' = 0.973 \pm 0.01$). The lower $Y_{500} - Y_X$ normalization for the full cluster sample results in $A' = 0.85^{+0.07}_{-0.08}$, which is in agreement with the measurement from S11.

Similarly, we compare the APEX-SZ $Y_{500} - M_{\text{gas}}$ and $Y_{500} - T_X$ best-fit normalizations to those in P11 and S10. For $Y_{500} - M_{\text{gas}}$ we measure a value of A consistent with S10 but 1.85σ higher than that of P11. For $Y_{500} - T_X$ the APEX-SZ result agrees with that of P11.

The level of intrinsic scatter in the $Y_{500} - Y_X$ relation for the REFLEX-DXL sample is similar to that observed by both P11 ($\sigma_{\log_{10}(Y)} = 0.10 \pm 0.01$) and S11 ($\sigma_{\log_{10}(Y)} = 0.09 \pm 0.04$). P11 also see an increased level of scatter for $Y_{500} - T_X$, however, the P11 scatter in $Y_{500} - M_{\text{gas}}$ is comparable to that of $Y_{500} - Y_X$.

In general, we find that our results from the REFLEX-DXL sample agree with previous measurements of SZE - X-ray scaling relations. The one notable exception is the normalization of the $Y_{500} - Y_X$ relation. For the full cluster sample, our results show some mild tension with both theoretical expectations and previous measurements in all three scaling relations parameters.

6. SYSTEMATIC UNCERTAINTIES

We divide our investigation of possible systematic contamination of these results into two categories: instrumental and analysis systematics and astrophysical ef-

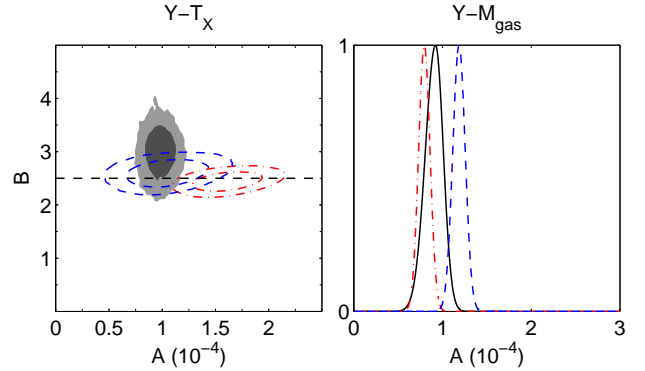


Figure 5. Likelihood constraints for the full cluster sample. The two-dimensional constraint for the normalization A and power exponent B is shown for the $Y_{500} - T_X$ relation in the left panel. The grey shaded areas represent the 68% and 95% confidence regions and the dashed straight line shows the self-similar value of the exponent. The $Y_{500} - M_{\text{gas}}$ constraint on A for the case where the exponent is fixed to the self-similar value ($B = 5/3$) is shown in the right panel. For comparison, the numerical results of Nagai (2006) for standard gas dynamics only (red/dash-dot) and cooling and feedback (blue/dashed) are shown in both panels.

fects. In the following two sections we discuss these systematics including the role of sample selection, correlations between the X-ray and SZE measurements, the effect of non-uniform X-ray measurements, known clusters that APEX-SZ did not detect, the assumptions inherent in the cluster profile modeling, contamination due to point sources, and an evolving gas mass fraction.

6.1. Instrumental and Analysis Uncertainties

6.1.1. Redshift Evolution

We find two main differences in the scaling relations between the REFLEX-DXL and full cluster samples. The exponent for the $Y_{500} - T_X$ relation is steeper and the intrinsic scatter in the $Y_{500} - Y_X$ relation increases for the full cluster sample. The REFLEX-DXL and full cluster samples are inherently different due to the contrasting sample selection methods (X-ray luminosity versus ad hoc). Therefore, it is not altogether surprising that measured scaling relations vary between the two samples. For example, one difference in the underlying population is the distribution of cluster redshifts. The full cluster sample extends to both low and high-redshifts, including five clusters at $z > 0.8$, while the REFLEX-DXL clusters are all chosen to have $z \sim 0.3$. Any redshift-dependent evolution in the scaling relations would exert more influence on the full cluster sample results than the REFLEX-DXL. We perform a simple test for bias introduced by including a broader redshift range. We repeat the regression analysis with the five high-redshift clusters excluded from the full cluster sample and find that they do not impact the measured scaling relations.

6.1.2. Correlated Scatter

A portion of the measured intrinsic scatter in $Y_{500} - T_X$ and $Y_{500} - Y_X$ can be attributed to correlation introduced by the fact that we use the X-ray temperature T_X to estimate r_{500} and therefore Y_{500} . We measure this correlation in the scaling relations by simulating the APEX-SZ dataset. For each cluster, a new temperature is drawn from its measured probability distribution and r_{500} is

Table 4
Scaling Relation Regression Parameters

Subset	N_{clusters}	Full Fit			N_{clusters}	Fixed Exponent		
		A	B	$\sigma_{\log_{10}(Y)}$		A	B	$\sigma_{\log_{10}(Y)}$
$Y - Y_X$								
REFLEX-DXL	11	$1.45^{+0.21}_{-0.20}$	$0.97^{+0.28}_{-0.31}$	$0.12^{+0.07}_{-0.05}$	11	$1.49^{+0.16}_{-0.19}$	1.00	$0.12^{+0.04}_{-0.05}$
All Clusters	35	$1.14^{+0.12}_{-0.11}$	$0.98^{+0.07}_{-0.12}$	$0.19^{+0.03}_{-0.02}$	35	$1.17^{+0.09}_{-0.12}$	1.00	$0.20^{+0.02}_{-0.02}$
Relaxed Only	17	$1.12^{+0.17}_{-0.21}$	$0.99^{+0.20}_{-0.22}$	$0.24^{+0.07}_{-0.05}$	17	$1.13^{+0.15}_{-0.22}$	1.00	$0.27^{+0.04}_{-0.07}$
Disturbed Only	17	$1.08^{+0.14}_{-0.11}$	$0.82^{+0.13}_{-0.10}$	$0.14^{+0.04}_{-0.04}$	17	$1.10^{+0.16}_{-0.11}$	1.00	$0.12^{+0.08}_{-0.01}$
$Y - M_{\text{gas}}$								
REFLEX-DXL	11	$1.32^{+0.31}_{-0.21}$	$1.08^{+0.47}_{-0.51}$	$0.18^{+0.06}_{-0.08}$	11	$1.54^{+0.27}_{-0.17}$	1.67	$0.13^{+0.02}_{-0.06}$
All Clusters	35	$0.94^{+0.11}_{-0.09}$	$1.16^{+0.10}_{-0.17}$	$0.24^{+0.03}_{-0.03}$	35	$0.92^{+0.09}_{-0.11}$	1.67	$0.23^{+0.02}_{-0.02}$
Relaxed Only	17	$0.92^{+0.20}_{-0.17}$	$1.23^{+0.38}_{-0.31}$	$0.30^{+0.07}_{-0.06}$	17	$0.93^{+0.26}_{-0.14}$	1.67	$0.34^{+0.05}_{-0.06}$
Disturbed Only	17	$0.90^{+0.13}_{-0.12}$	$1.06^{+0.17}_{-0.18}$	$0.20^{+0.06}_{-0.04}$	17	$0.85^{+0.14}_{-0.11}$	1.67	$0.22^{+0.03}_{-0.02}$
$Y - T_X$								
REFLEX-DXL	11	$1.11^{+0.20}_{-0.16}$	$2.00^{+0.67}_{-0.76}$	$0.17^{+0.06}_{-0.04}$	11	$1.06^{+0.16}_{-0.13}$	2.50	$0.16^{+0.06}_{-0.04}$
All Clusters	42	$0.96^{+0.11}_{-0.07}$	$3.04^{+0.29}_{-0.35}$	$0.21^{+0.02}_{-0.06}$	42	$0.98^{+0.09}_{-0.11}$	2.50	$0.20^{+0.06}_{-0.02}$
Relaxed Only	20	$1.04^{+0.16}_{-0.15}$	$3.60^{+0.63}_{-0.63}$	$0.16^{+0.08}_{-0.04}$	20	$0.99^{+0.18}_{-0.15}$	2.50	$0.24^{+0.05}_{-0.06}$
Disturbed Only	19	$1.00^{+0.14}_{-0.10}$	$2.58^{+0.47}_{-0.44}$	$0.16^{+0.05}_{-0.04}$	19	$1.03^{+0.11}_{-0.12}$	2.50	$0.16^{+0.05}_{-0.04}$

Note. — The values of A presented in this table are in units of 10^{-4} .

determined from the $r_{500} - T$ relation. The Y_{500} distributions are recalculated and the regression analysis is performed on each realization of the scaling relation. We find that this correlation accounts for an intrinsic scatter of $\sim 7.1\%$ in the scaling relations, which is small in comparison to the total measured scatter.

6.1.3. Non-Uniform X-ray Analysis

The X-ray observables used in the APEX-SZ scaling relations are drawn from several different pre-existing studies in the literature. The REFLEX-DXL clusters are the exception, as their X-ray parameters are taken from a single study and uniformly analyzed. Subtle differences between X-ray analyses translate into both a systematic bias and increased uncertainty in Y_{500} scaling relations for the full APEX-SZ sample.

Plagge et al. (2010) used X-ray observables from several different studies and found that the measured $Y_{500} - M_{\text{gas}}$, and by extension, $Y_{500} - Y_X$ relations changed significantly depending on the choice of study. Rozo et al. (2014b) compared hydrostatic mass estimates of common clusters in three different X-ray samples. These authors found total mass differences as large as 45% at a redshift of 0.2, resulting in differences in r_{500} and the aperture used to measure M_{gas} and T_X . These aperture differences are in addition to those regarding the specific fraction of r_{500} (e.g., $0.15 - 1r_{500}$) used by individual authors for T_X measurements (see the note in Table 2). For cool-core clusters in particular the core region is known to bias estimates of the cluster temperature and is often excluded, but the exact boundary chosen varies between authors. Additionally, the outer radius is often determined by data quality limitations.

Rozo et al. (2012) measured Y_X from Chandra observations for a subset of the clusters in Planck Collaboration XI (2011) and compared these data with the *Planck*

SZE measurements to constrain the $Y_{500} - Y_X$ relation. These authors found a significantly lower level of intrinsic scatter in comparison with the original *Planck* + *XMM-Newton* analysis of the full sample ($8.2 \pm 3.5\%$ and $22.8 \pm 2.3\%$, respectively). When considering the same subset of clusters as the Chandra analysis, Rozo et al. (2012) measure a $16.7 \pm 3.9\%$ intrinsic scatter. Rozo et al. (2014a) extends this analysis by comparing *Planck* data (Planck Collaboration XI 2011) with Y_X from Mantz et al. (2010a) and suggest an upper limit on the intrinsic scatter of 15%. These authors conclude that the observed variations are the result of systematic differences in the X-ray analysis.

We investigate the importance of uniform X-ray analysis by analyzing subsets of the full APEX-SZ cluster sample which have X-ray parameters from a single study. There are three divisions that make up the bulk of the sample: Zhang et al. (2008), Zhang et al. (2006, the REFLEX-DXL sample), and Mantz et al. (2010a). We find that there are significant variations in both the normalization and exponent for the $Y_{500} - T_X$ relation between the three independent subsets. The $Y_{500} - M_{\text{gas}}$ relation has less variation in the exponent, while the normalization changes by a factor of two between the Zhang et al. (2008) and Mantz et al. (2010a) subsamples. The $Y_{500} - Y_X$ relation shows a similar factor of two variation in the normalization.

For all three scaling relations, we find the measured intrinsic scatter for a uniformly analyzed subset is less than that for the full sample. The most dramatic improvement in scatter is seen for the Mantz et al. (2010a) sample, decreasing for the $Y_{500} - T_X$ relation from 44% to 12%. By drawing random sets of clusters from the full sample and performing the regression analysis, we conclude that this level of scatter has a 1% chance of occurring based on the parent distribution and that the observed decrease

in intrinsic scatter is significant. Overall, we find that using X-ray parameters from multiple studies introduces significant variability and uncertainty in the power law parameters due to systematic analysis differences. Additionally, the intrinsic scatter is dominated by systematics when using multiple studies. Therefore, we do not draw strong conclusions from the full cluster sample.

6.1.4. Cluster Non-Detections

Beyond the challenges of the non-uniform X-ray analysis, there are six clusters in the full sample that APEX-SZ did not detect (defined by $Y_{500} < \sigma_{Y_{500}}$). These clusters are specified in Table 3. Included in the non-detections are the three clusters with the highest redshifts: RDCSJ1252-2927 ($z = 1.240$), XMMXCSJ2215.9-1738 ($z = 1.45$), and XMMUJ2235.3-2557 ($z = 1.393$). These clusters were also observed at 31 GHz by Culverhouse et al. (2010) using the Sunyaev-Zel'dovich Array (SZA). Of the three, only XMMUJ2235.3-2557 was detected by SZA. The APEX-SZ Y_{500} likelihood distributions for RDCSJ1252-2927 and XMMXCSJ2215.9-1738 are consistent with the SZA upper limits. Culverhouse et al. (2010) conclude that RDCSJ1252-2927 and XMMXCSJ2215.9-1738 are lower mass systems than expected from X-ray measurements.

We calculate the PTE of the measured Y_{500} for each cluster given the probability distribution of the best-fit scaling relation with log-normal scatter. In the case where Y_{500} is unbiased for all clusters, the distribution of PTEs will be consistent with a uniform distribution. We find that without the non-detections, comparing this distribution to a uniform distribution results in a PTE of 24%, indicating that the two are consistent. In comparison, when the non-detections are included the PTE drops to 3%, indicating that the non-detections are in tension with the best-fit scaling relation.

We investigate the influence of the non-detections by comparing the measured scaling relation regression parameters with and without the non-detections included. In general, the maximum likelihood parameters for the full cluster sample change at approximately the 1σ level. The one exception is for the $Y_{500} - Y_X$ exponent, which decreases by $\sim 2\sigma$ when non-detections are excluded. For all three scaling relations, the intrinsic scatter decreases slightly when excluding the non-detections. Overall, we conclude that the non-detections are not a significant driving factor for the scaling relations with the full cluster sample.

6.1.5. Pressure Profile Model

A final analysis systematic to consider is the assumption that the Arnaud et al. (2010) model with our inferred values of r_{500} accurately represents the true cluster pressure profile. Andersson et al. (2011) find that Y_{500} varies by $\sim 10\%$ under a variety of model assumptions, including the Arnaud et al. (2010) profile. The limited angular extent and strong timestream filtering of the APEX-SZ data prevent us from exploring different model parametrizations. However, we list the PTE for the Arnaud et al. (2010) model fit to each cluster in Table 3. If we exclude clusters which have a poor fit to the chosen Arnaud et al. (2010) model ($\sim 25\%$ of the sample with $\text{PTE} < 1\%$ or $\text{PTE} > 99\%$), the power law regression parameters do not change significantly.

6.2. Astrophysical Uncertainties

6.2.1. Point Sources

At the APEX-SZ observing frequency, emission from point sources can mask the SZE signal from a cluster. We estimate the effect of radio sources by extrapolating the flux densities of sources in the NRAO VLA Sky Survey (1.4 GHz, Condon et al. 1998), VLA FIRST (1.4 GHz, Becker et al. 1995), and Parkes-MIT-NRAO (4.85 GHz, Griffith & Wright 1993) surveys to 150 GHz. Assuming a power law spectral energy distribution, $S \sim \nu^\alpha$, with $\alpha = -0.7$, there are six clusters with known bright sources with $\Delta T_{\text{CMB}} > 100 \mu\text{K}$ within two arcminutes of the X-ray centroid. Of these six, two (RXCJ2014.8-2430 and MACSJ1931.8-2635) are not detected by APEX-SZ.

Simulations from Sehgal et al. (2010) suggest that only 1% of clusters with masses similar to those observed in this paper will have radio sources at 150 GHz that contaminate the integrated cluster signal by 20% or more. For the APEX-SZ clusters, this implies that a single cluster would suffer from radio contamination and that our estimate of six contaminated clusters is extremely conservative.

We have also observed a subset of the APEX-SZ clusters with the CARMA array, searching for point source contamination. Nine clusters were observed at 100 GHz and three at 230 GHz with an average map rms of approximately 0.9 and 4.4 mJy/beam, respectively. We detect a 7.4 mJy source at 100 GHz in the map of RXCJ1504.1-0248. Of the three non-detection clusters observed with CARMA (XMMUJ2235.3-2557, XMMXCSJ2215.9-1738, XMMUJ1230.3+1339) no point sources are detected.

We test for the effects of the six bright point sources by excluding the associated clusters from the full cluster sample. There is no significant difference in the measured scaling relations parameters when removing these potentially contaminated clusters.

6.2.2. Evolving Gas Mass Fraction

The final systematic we investigate is a gas mass fraction that evolves as a function of total mass. There is evidence in both observations (Zhang et al. 2006; Vikhlinin et al. 2009a) and simulations (Battaglia et al. 2013) that the gas mass fraction evolves due to the thermodynamics and feedback processes in the intracluster medium. As seen in Equation 4, both the $Y_{500} - T_X$ and $Y_{500} - M_{\text{gas}}$ relation depend on the gas mass. All of the results presented in Table 4 assume a constant gas mass fraction embedded in the normalization term. We test the effect of an evolving gas mass fraction by first estimating cluster mass using a scaling relation with T_X from Vikhlinin et al. (2009a). We adopt the functional form for gas mass fraction given by the same authors, $f_{\text{gas}}(h/0.72)^{1.5} = 0.125 + 0.037 \cdot \log(M_{15})$, where M_{15} is the total cluster mass M_{500} in units of $10^{15} h^{-1} M_\odot$. We then look for the effect of evolving f_{gas} on the power law exponent parameter in the measured scaling relations.

When accounting for the evolving f_{gas} we find a $Y_{500} - M_{\text{gas}}$ power law exponent of $B = 1.35_{-0.56}^{+0.42}$ for the REFLEX-DXL sample and $B = 1.08_{-0.12}^{+0.38}$ for the full sample, both of which are consistent with the results where we assume a constant f_{gas} , and are consistent with

self-similarity. In addition, the intrinsic scatter increases from $\sigma_{\log_{10}(Y)} = 0.13(0.23)$ to $\sigma_{\log_{10}(Y)} = 0.17(0.37)$ for the REFLEX-DXL (full) sample. However, the stated uncertainty in the f_{gas} relation is $\sim 4 - 5\%$ (Vikhlinin et al. 2009b) and our use of T_X combined with the scatter already present in the $Y_{500} - M_{gas}$ relation most likely explains the increase.

In summary, we examine the role of millimeter-wavelength point sources and an evolving gas mass fraction as astrophysical systematics in the APEX-SZ scaling relations. We find no evidence for bias or additional intrinsic scatter due to point sources. Accounting for an evolving gas mass fraction results in a slight change to the measured power law and increases the intrinsic scatter.

6.3. Dynamical State

As discussed in the previous two sections, the full cluster sample is affected by several systematics that prevent rigorous interpretation of the results. Nevertheless, the sample was selected independently of dynamical state and we can examine the influence it has on the Y_{500} scaling relations. We use cluster morphology as an indicator of dynamical state. Clusters are divided into three subsets based on literature morphological classification from X-ray images: *relaxed*, *disturbed*, and *unknown*. Relaxed clusters exhibit symmetric contours that are centered around the peak in X-ray brightness. A cool-core is often used as an indicator of relaxation. Disturbed clusters exhibit significant substructure. In the extreme case of a recent major merger, disturbed clusters can exhibit multiple distinct components in the ICM. A cluster is also classified as disturbed if there is significant ellipticity or an offset X-ray centroid. Morphological classifications are given in Table 2. In a handful of cases, morphological information is unknown due a lack of detailed observations.

Regression analysis is performed on the relaxed and disturbed subsets separately and the resulting regression parameters are given in Table 4. It is important to note that these results will include any morphological dependencies in the X-ray observables (Kravtsov et al. 2006; Nagai et al. 2007b) as well as the SZE. Compared to the results from the full sample, neither the relaxed nor the disturbed clusters exhibit significant change in the power law exponents. Overall, this agrees with numerical predictions that integrated- Y is insensitive to dynamical state (Wik et al. 2008).

In the $Y_{500} - Y_X$ relation, the intrinsic scatter is lower for the disturbed clusters at a level that occurs only 1% of the time given the parent distribution. This is counter intuitive as relaxed clusters are by definition closer to being in a state of hydrostatic equilibrium, the underlying assumption upon which scaling relations are based. We attribute this behavior to the scatter between parameters from different X-ray studies, since the majority of the disturbed clusters have M_{gas} from a single study while the relaxed clusters are split between three studies.

7. SUMMARY

We present Sunyaev-Zel'dovich effect (SZE) observations of galaxy clusters measured with the APEX-SZ experiment and use them to investigate the scaling of

the SZE with cluster mass. We model the thermal pressure of the intracluster medium using the Arnaud et al. (2010) universal pressure profile and use the results to calculate the spherical integrated Comptonization Y_{500} for each cluster. We compare these measurements of Y_{500} to X-ray estimates of cluster mass taken from the literature. Using these two sets of observables, we measure the $Y_{500} - Y_X$, $Y_{500} - M_{gas}$, and $Y_{500} - T_X$ scaling relations, finding the best-fit power law and intrinsic scatter for each. These scaling relations are measured for both the X-ray luminous REFLEX-DXL cluster sample as well as the full APEX-SZ sample of 42 clusters.

The full cluster sample, which includes the REFLEX-DXL clusters, is one of the larger samples used to measure SZE scaling relations to date. However, it has an *ad hoc* selection function as well as a non-uniform X-ray analysis. We find that the systematics introduced by these aspects of the sample create significant variations in the power law regression parameters and increases the intrinsic scatter. Therefore we do not draw any strong conclusions from the scaling relations for the full cluster sample.

For the REFLEX-DXL sample, we find that the best-fit power laws for the $Y_{500} - Y_X$, $Y_{500} - M_{gas}$, and $Y_{500} - T_X$ relations have exponents consistent with those predicted by the self-similar model. We compare the measured normalizations for each scaling relation to numerical simulations to probe the underlying astrophysics of the intracluster medium (ICM). The measured normalization for the $Y_{500} - Y_X$ relation implies a higher $Y_{500}d_A^2/Y_X$ than seen in previous studies. However, we find large variations in the measured normalization when dividing the full sample into subsets with uniformly analyzed X-ray data, including the REFLEX-DXL sample. Therefore, we associate a large systematic uncertainty with the high $Y_{500}d_A^2/Y_X$ and do not draw further conclusions from it. We compare the normalization for the $Y_{500} - M_{gas}$ and $Y_{500} - T_X$ relations to the numerical simulations of Nagai (2006) and find a weak preference for models that included radiative cooling and feedback in the ICM as well as standard gas dynamics.

Finally, we find that the intrinsic scatter is the lowest for the $Y_{500} - Y_X$ relations, $\sigma_{\log_{10}(Y)} = 0.12^{+0.07}_{-0.05}$ ($\sim 28^{+16}_{-12}\%$). The uncertainties in the intrinsic scatter are large due to the small number of clusters in the REFLEX-DXL sample. A larger sample is key to improving this measurement of intrinsic scatter in Y_{500} and its application as an estimator for total cluster mass in cluster-based cosmological constraints.

A uniform X-ray analysis for the full sample APEX-SZ clusters is ongoing. This analysis will resolve the main systematic limitation of the full cluster sample and will allow us to use its large number of clusters to improve on the constraints presented here for the REFLEX-DXL sample. Additionally, a follow-up program of optical observations has been concluded to estimate the total cluster mass independently using weak-lensing measurements. Future papers will use the additional X-ray and weak-lensing information to improve further our understanding of how Y_{500} scales with total cluster mass and facilitate its use in exploring the physics of the ICM as well as in constraining cosmological parameters using galaxy clusters.

We thank the staff at the APEX telescope site, at the time of observations led by David Rabanus and previously by Lars-Åke Nyman, for their dedicated and exceptional support. We also thank Bradford Benson for useful comments on a draft version of the manuscript as well as LBNL engineers John Joseph and Chinh Vu for their work on the readout electronics. APEX-SZ is funded by the National Science Foundation under Grant Nos. AST-0138348 & AST-0709497. Work at LBNL is supported by the Director, Office of Science, Office of High Energy and Nuclear Physics, of the U.S. Department of Energy under Contract No. DE-AC02-05CH11231. Work at McGill is supported by the Natural Sciences and Engineering Research Council of Canada, the Canada Research Chairs program, and the Canadian Institute for Advanced Research. This work has been partially supported by the DFG Transregio program TR33 "The Dark Universe". FP acknowledges support from the BMBF/DLR grant Nr. 50 OR 1117. CH acknowledges support from the Barbro Osher pro Suecia foundation and from the Swedish Research Council under grants 2006-3356 and 2009-4027. NWH acknowledges support from the Alfred P. Sloan Foundation.

REFERENCES

- Allen, S. W., Rapetti, D. A., Schmidt, R. W., et al. 2008, *MNRAS*, 383, 879
- Andersson, K., Peterson, J. R., Madejski, G., & Goobar, A. 2009, *ApJ*, 696, 1029
- Andersson, K., Benson, B. A., Ade, P. A. R., et al. 2011, *ApJ*, 738, 48
- Arnaud, M., Pratt, G. W., Piffaretti, R., et al. 2010, *A&A*, 517, A92+
- Battaglia, N., Bond, J. R., Pfrommer, C., & Sievers, J. L. 2013, *ApJ*, 777, 123
- Becker, R. H., White, R. L., & Helfand, D. J. 1995, *ApJ*, 450, 559
- Benson, B. A., de Haan, T., Dudley, J. P., et al. 2013, *ApJ*, 763, 147
- Böhringer, H., Schuecker, P., Guzzo, L., et al. 2004, *A&A*, 425, 367
- Bonamente, M., Joy, M., LaRoque, S. J., et al. 2008, *ApJ*, 675, 106
- Branchesi, M., Gioia, I. M., Fanti, C., & Fanti, R. 2007, *A&A*, 472, 727
- Carlstrom, J. E., Ade, P. A. R., Aird, K. A., et al. 2011, *PASP*, 123, 568
- Condon, J. J., Cotton, W. D., Greisen, E. W., et al. 1998, *AJ*, 115, 1693
- Culverhouse, T. L., Bonamente, M., Bulbul, E., et al. 2010, *ApJ*, 723, L78
- De Filippis, E., Bautz, M. W., Sereno, M., & Garmire, G. P. 2004, *ApJ*, 611, 164
- Demarco, R., Rosati, P., Lidman, C., et al. 2007, *ApJ*, 663, 164
- Dobbs, M., Halverson, N. W., Ade, P. A. R., et al. 2006, *New Astronomy Review*, 50, 960
- Dobbs, M. A., Lueker, M., Aird, K. A., et al. 2012, *Review of Scientific Instruments*, 83, 073113
- Ebeling, H., Barrett, E., Donovan, D., et al. 2007, *ApJ*, 661, L33
- Ebeling, H., Edge, A. C., Mantz, A., et al. 2010, *MNRAS*, 407, 83
- Fassbender, R., Böhringer, H., Santos, J. S., et al. 2011, *A&A*, 527, A78+
- Gilbank, D. G., Gladders, M. D., Yee, H. K. C., & Hsieh, B. C. 2011, *AJ*, 141, 94
- Govoni, F., Markevitch, M., Vikhlinin, A., et al. 2004, *ApJ*, 605, 695
- Griffin, M. J., & Orton, G. S. 1993, *??jnlIcarus*, 105, 537
- Griffith, M. R., & Wright, A. E. 1993, *AJ*, 105, 1666
- Güsten, R., Booth, R. S., Cesarsky, C., et al. 2006, in *Society of Photo-Optical Instrumentation Engineers (SPIE) Conference Series*, Vol. 6267, Society of Photo-Optical Instrumentation Engineers (SPIE) Conference Series
- Haiman, Z., Mohr, J. J., & Holder, G. P. 2001, *ApJ*, 553, 545
- Hall, N. R., Keisler, R., Knox, L., et al. 2010, *ApJ*, 718, 632
- Hallman, E. J., Motl, P. M., Burns, J. O., & Norman, M. L. 2006, *ApJ*, 648, 852
- Halverson, N. W., Lanting, T., Ade, P. A. R., et al. 2009, *ApJ*, 701, 42
- Hasselfield, M., Hilton, M., Marriage, T. A., et al. 2013, *??jnlJ. Cosmology Astropart. Phys.*, 7, 8
- Hezaveh, Y., Vanderlinde, K., Holder, G., & de Haan, T. 2013, *ApJ*, 772, 121
- Hinshaw, G., Weiland, J. L., Hill, R. S., et al. 2009, *ApJS*, 180, 225
- Kaiser, N. 1986, *MNRAS*, 222, 323
- Kelly, B. C. 2007, *ApJ*, 665, 1489
- Komatsu, E., Smith, K. M., Dunkley, J., et al. 2011, *ApJS*, 192, 18
- Krause, E., Pierpaoli, E., Dolag, K., & Borgani, S. 2012, *MNRAS*, 419, 1766
- Kravtsov, A. V., Vikhlinin, A., & Nagai, D. 2006, *ApJ*, 650, 128
- Lau, E. T., Kravtsov, A. V., & Nagai, D. 2009, *ApJ*, 705, 1129
- Lee, A. T., Richards, P. L., Nam, S. W., Cabrera, B., & Irwin, K. D. 1996, *Applied Physics Letters*, 69, 1801
- Mantz, A., Allen, S. W., Ebeling, H., Rapetti, D., & Drlica-Wagner, A. 2010a, *MNRAS*, 406, 1773
- Mantz, A., Allen, S. W., Rapetti, D., & Ebeling, H. 2010b, *MNRAS*, 406, 1759
- Marriage, T. A., Acquaviva, V., Ade, P. A. R., et al. 2011, *ApJ*, 737, 61
- Marrone, D. P., Smith, G. P., Okabe, N., et al. 2012, *ApJ*, 754, 119
- Maughan, B. J., Jones, C., Forman, W., & Van Speybroeck, L. 2008, *ApJS*, 174, 117
- Mehrtens, N., Romer, A. K., Hilton, M., et al. 2012, *MNRAS*, 423, 1024
- Motl, P. M., Hallman, E. J., Burns, J. O., & Norman, M. L. 2005, *ApJ*, 623, L63
- Muhleman, D. O., & Berge, G. L. 1991, *Icarus*, 92, 263
- Mullis, C. R., Rosati, P., Lamer, G., et al. 2005, *ApJ*, 623, L85
- Nagai, D. 2006, *ApJ*, 650, 538
- Nagai, D., Kravtsov, A. V., & Vikhlinin, A. 2007a, *ApJ*, 668, 1
- Nagai, D., Vikhlinin, A., & Kravtsov, A. V. 2007b, *ApJ*, 655, 98
- Navarro, J. F., Frenk, C. S., & White, S. D. M. 1997, *ApJ*, 490, 493
- Nolta, M. R., Dunkley, J., Hill, R. S., et al. 2009, *ApJS*, 180, 296
- Nozawa, S., Itoh, N., Kawana, Y., & Kohyama, Y. 2000, *The Astrophysical Journal*, 536, 31
- Pacaud, F., Pierre, M., Adami, C., et al. 2007, *MNRAS*, 382, 1289
- Pardo, J. R., Cernicharo, J., & Serabyn, E. 2001, *IEEE Transactions on Antennas and Propagation*, 49, 1683
- Plagge, T., Benson, B. A., Ade, P. A. R., et al. 2010, *ApJ*, 716, 1118
- Planck Collaboration XI. 2011, *A&A*, 536, A11
- Planck Collaboration XXIX. 2013, *ArXiv e-prints*, arXiv:1303.5089
- Pratt, G. W., Croston, J. H., Arnaud, M., & Böhringer, H. 2009, *A&A*, 498, 361
- Press, W. H., Teukolsky, S. A., Vetterling, W. T., & Flannery, B. P. 2007, *Numerical Recipes: The Art of Scientific Computing*, 3rd edn. (Cambridge: Cambridge University Press)
- Reichardt, C. L., Stalder, B., Bleem, L. E., et al. 2013, *ApJ*, 763, 127
- Rosati, P., Tozzi, P., Gobat, R., et al. 2009, *A&A*, 508, 583
- Rozo, E., Evrard, A. E., Rykoff, E. S., & Bartlett, J. G. 2014a, *MNRAS*, 438, 62
- Rozo, E., Rykoff, E. S., Bartlett, J. G., & Evrard, A. 2014b, *MNRAS*, 438, 49
- Rozo, E., Vikhlinin, A., & More, S. 2012, *ApJ*, 760, 67
- Rudy, D. J., Muhleman, D. O., Berge, G. L., Jakosky, B. M., & Christensen, P. R. 1987, *Icarus*, 71, 159
- Sayers, J. 2007, PhD thesis, California Institute of Technology
- Sayers, J., Golwala, S. R., Ameglio, S., & Pierpaoli, E. 2011, *ApJ*, 728, 39

- Schwan, D., Ade, P. A. R., Basu, K., et al. 2011, Review of Scientific Instruments, 82, 091301
- Sehgal, N., Bode, P., Das, S., et al. 2010, ApJ, 709, 920
- Shirokoff, E., Reichardt, C. L., Shaw, L., et al. 2011, ApJ, 736, 61
- Sifón, C., Menanteau, F., Hasselfield, M., et al. 2013, ApJ, 772, 25
- Sunyaev, R. A., & Zel'dovich, Y. B. 1972, Comments on Astrophysics, 4, 173
- Swetz, D. S., Ade, P. A. R., Amiri, M., et al. 2011, ApJS, 194, 41
- Vikhlinin, A., Kravtsov, A., Forman, W., et al. 2006, ApJ, 640, 691
- Vikhlinin, A., Burenin, R. A., Ebeling, H., et al. 2009a, ApJ, 692, 1033
- Vikhlinin, A., Kravtsov, A. V., Burenin, R. A., et al. 2009b, ApJ, 692, 1060
- Weiland, J. L., Odegard, N., Hill, R. S., et al. 2011, ApJS, 192, 19
- Weiner, B. J., Willmer, C. N. A., Faber, S. M., et al. 2006, ApJ, 653, 1049
- Weller, J., Battye, R. A., & Kneissl, R. 2002, Physical Review Letters, 88, 231301
- Wik, D. R., Sarazin, C. L., Ricker, P. M., & Randall, S. W. 2008, ApJ, 680, 17
- Zhang, Y.-Y., Böhringer, H., Finoguenov, A., et al. 2006, A&A, 456, 55
- Zhang, Y.-Y., Finoguenov, A., Böhringer, H., et al. 2008, A&A, 482, 451